Available online at www.sciencedirect.com
SCIENCE DIRECT®
PERGAMON
International Journal of Heat and Mass Transfer 46 (2003) 4157–4168
International Journal of HEAT and MASS TRANSFER
www.elsevier.com/locate/ijhmt

Chemical reacting transport phenomena in a PEM fuel cell

Tien-Chien Jen [a,*], Tuanzhou Yan [a], Shih-Hung Chan [b]

[a] Department of Mechanical Engineering, University of Wisconsin at Milwaukee, Milwaukee, WI 53211, USA
[b] The Office of the President Yuan-Ze University, Chung-Li, Taoyuan, 320, Taiwan

Received 18 October 2002; received in revised form 28 April 2003

Abstract

A three-dimensional mathematical model for the PEM fuel cell including gas channel has been developed to simulate fuel cell performance. A set of conservation equations and species concentration equations are solved numerically in a coupled gas channel and porous media domain using the vorticity–velocity method with power law scheme. Detailed development of axial velocity and secondary flow fields are presented at various axial locations. Polarization curves are demonstrated by solving the equations for electrochemical reactions and the membrane phase potential. Compared with experimental data from published literatures, numerical results of this model agree closely with experimental results.

Keywords: Fuel cell; Semi-porous media; Numerical analysis

1. Introduction

With the increasing environmental concerns on the vehicle-generated pollution and the waste of nuclear power plants, the fuel cell system is gaining more attention as an alternative electric power source. The most significant advantages associated with fuel cells are that they are not limited by Carnot efficiency. No gases are heated to create explosive reactants, and no moving parts similar to pistons and crankshafts are required to convert thermal energy to mechanical energy. The energy released from the inter-atomic bonds of the reactants is converted more efficiently into usable electrical energy relative to traditional power generation devices. Due to these advantages, fuel cell engines can potentially replace the internal combustion engine for transportation and nuclear power plants.

Although the fuel cell has received much attention in recent years, the underlying concept is still under heavy investigations [1]. The general concept of fuel cell operation can be characterized as gas-mixtures transport and transformation of species by electrochemical reactions. Therefore, one of the most challenging problems in fuel cell research is to predict the performance of the fuel cell. Using a mathematical model with numerical procedures to simulate the transport phenomena is a powerful way to understand the fundamental physical and chemical processes of a fuel cell.

Detailed reviews of hydrogen PEM fuel cell research can be found in [2,3]. In previous studies, most models focused only on one-dimensional flow [4–11]. Most of these models treated flow channel as being perfectly well fixed, with no pressure and concentration difference along the gas channel. These research works were particularly useful in classifying the different models for porous gas diffusion electrodes and providing the key properties of the membrane required for numerical simulation. Ticianelli et al. [12,13] published comprehensive experimental study. Their experimental data have been used as standard validation by many other numerical studies such as [11,14].

Later, two-dimensional (2-D) models are developed to improve the earlier one-dimensional (1-D) models. These works can be found in [14–17]. These 2-D models provide more realistic numerical simulation of the fuel cell performance.

* Corresponding author. Tel.: +1-414-229-2307; fax: +1-414-229-6958.
E-mail address: jen@cae.uwm.edu (T.-C. Jen).

0017-9310/$ - see front matter © 2003 Elsevier Ltd. All rights reserved.
doi:10.1016/S0017-9310(03)00253-9

Nomenclature

A	cross-section area, cm^2
D_e	hydraulic diameter, $4A/S$, cm
D_k	diffusion coefficient of the kth component, cm^2/s
$D_{eff,k}$	effective diffusion coefficient of the kth component in the porous media, cm^2/s
E^o	thermodynamic open circuit potential, V
F	Faraday constant, C/mol
I	operating cells current density, A/cm^2
T	temperature, K
Pe	Peclet number
R	gas constant, J/mol K
Re	Reynolds number
Sc_k	Schmidt number for species k
X	species mole fraction
$x^{ref}_{H_2}$	H_2 reference molar fraction
$x^{ref}_{O_2}$	O_2 reference molar fraction
a	vapor activity
$aj^{ref}_{0,a}$	reference exchange current density times area of anode, A/cm^3
$aj^{ref}_{0,c}$	reference exchange current density times area of anode, A/cm^3
c_{tota}	total anode mole concentration, $mole/cm^3$
c_{totc}	total cathode mole concentration, $mole/cm^3$
f	friction factor
j	transfer current density, A/cm^3
u, v, w	velocity in x-, y-, z-direction, cm/s
p	pressure, Pa
z_f	Fixed site charge

Greek symbols

α_a	anode transfer coefficient
α_c	cathode transfer coefficient
ε	porosity
ε_m	membrane porosity
ε_{mc}	membrane volume fraction
σ_m	ionic conductivity, mho/cm
ρ	density, g/cm^3
κ	permeability, cm^2
Φ	cell potential, J/mol K
v	kinematical viscosity, cm^2/s
μ	dynamic viscosity, g/cm s
ζ	vorticity
η	overpotential, V

Superscript

–	non-dimensional variable

Subscripts

a	anode
avg	average
c	cathode
i	inlet condition
k	kth component
m	membrane
w	water

Recently, Yi and Nguyen [18] modified the previous model to include heat and mass transfer conditions in both the liquid and gas phases along the flow path of the fuel cell. Shimpalee and Dutta [19] described a steady state, isothermal, three-dimensional, and single phase PEM fuel cell model. This work was the first three-dimensional (3-D) model used to predict the performance of a fuel cell. They used FLUENT to solve the complete Navier–Stokes equations. More recently, Zhou and Liu [20], Um and Wang [21,22] described a 3-D model for PEM fuel cell. Non-dimensional forms of the governing equations were developed and the effects of dimensionless parameters on fuel cell performance were evaluated. Their results agree well with their own experimental observations.

The objective of this study is to develop a single-phase, multi-species, three-dimensional mathematical model for electrochemical kinetics, current density distribution, fluid flow, and multi-component transport in fuel cell. This model was solved numerically using a vorticity–velocity method with power-law scheme. There are some extensive literatures dedicated to flow in this kind of semi-porous media. A detailed literature review on the flow development in semi-porous media and descriptions of the vorticity–velocity method with power-law scheme can be found in [23].

In this study, the formulations are developed in such a way that they allow using the same code for solving the Navier–Stokes equations of the gas channel, gas diffuser and catalyst layers in a coupled domain. The potential equation and species equations are solved in a single domain of whole fuel cell. The solutions of the hydrodynamics of the flow and polarization curves are analyzed and presented in detail. The results of this study will be beneficial for further and more complete analyses of the performance of fuel cells.

2. Model development

A typical PEM fuel cell configuration is shown in Fig. 1. The physical fuel cell model consists of anode gas channel, anode gas diffuser that formed by porous media, anode catalyst layer, membrane, cathode catalyst layer, cathode gas diffuser, and cathode gas channel as shown in Fig. 1. In reality, when the fuel cell works, fuel

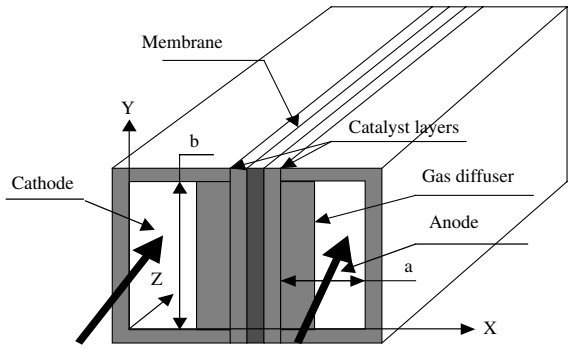

Fig. 1. Fuel cell configuration.

and oxidant can be viewed as a steady, laminar, developing forced convection flow in an isothermal rectangular channel, and penetrating through the gas diffuser to catalyst layers. A uniform inlet axial velocity $W_i = W_0$ is imposed at $Z = 0$. The duct wall temperature is held constant at T_w. The flow is assumed to be steady, constant property, and incompressible. The axial diffusion, viscous dissipation, compression work and buoyancy are assumed negligible. The gas mixtures are considered as perfect gases, and the species concentrations are considered as constant at the inlet of the channel. The concentrations along the gas channel and the gas-diffuser will vary due to diffusion-convection transport and electron kinetics in catalyst layers, and the distributions will depend on the gas properties and reaction rate. Water transport in and out of the electrodes is assumed to be in the form of vapor only. This assumption may be questionable in this model, in particular when the reactants flow into the gas channel with saturated conditions. The water generation rate is very likely to exceed its removal rate and thus condensation formed in cathode. As a result, two-phase flow forms in the cathode channel. This complex case is, however, neglected in this study. The gas-diffuser, catalyst layers, and the membrane materials are considered as isotropic porous media. Contraction of the porous media is also neglected.

The fluid flow in the gas channel is described by the continuity and Navier–Stokes equations. The axial and cross-sectional pressure gradients may be decoupled by making the usual parabolic assumption [24]. A modified pressure P may be defined as

$$P(X, Y, Z) = p(Z) + p^*(X, Y), \tag{1}$$

where $p(Z)$ is the pressure over the cross-section at each axial location, and $p'(X, Y)$ is the pressure variation in the X, Y direction, which drives the secondary flow. Pressure gradient for axial direction:

$$\frac{\partial P}{\partial Z} = \frac{\partial p}{\partial Z} + \frac{\partial p^*}{\partial Z}, \tag{2}$$

where $\partial p/\partial Z \gg \partial p^*/\partial Z$ is due to the parabolic assumption. So the axial pressure gradient can be written as:

$$\frac{\partial P}{\partial Z} = \frac{\partial p}{\partial Z} = f(Z). \tag{3}$$

And we also have:

$$\frac{\partial P}{\partial X} = \frac{\partial p^*}{\partial X}, \tag{4}$$

$$\frac{\partial P}{\partial Y} = \frac{\partial p^*}{\partial Y}. \tag{5}$$

The following dimensionless variables and parameters are introduced:

$$D_e = \frac{4A}{S}, \quad \bar{u} = \frac{U}{U_i}, \quad \bar{v} = \frac{V}{U_i}, \quad \bar{w} = \frac{W}{U_c}, \quad \bar{x} = \frac{X}{D_e},$$
$$\bar{y} = \frac{Y}{D_e}, \quad \bar{z} = \frac{Z}{D_e Re}, \quad \bar{p} = \frac{P - P_i}{\rho_i U_i^2}, \quad Re = \frac{\rho_i U_i D_e}{\mu},$$
$$\bar{\kappa} = \frac{\kappa}{D_e^2}, \quad S_{Ck} = \frac{\mu}{\rho D_k}, \quad U_c = U_i Re. \tag{6}$$

2.1. In the gas channels

Following the parabolic assumption, the governing equations are as follows:

$$\frac{\partial \bar{u}}{\partial \bar{x}} + \frac{\partial \bar{v}}{\partial \bar{y}} + \frac{\partial \bar{w}}{\partial \bar{z}} = 0, \tag{7}$$

$$Re\left(\bar{u}\frac{\partial \bar{v}}{\partial \bar{x}} + \bar{v}\frac{\partial \bar{v}}{\partial \bar{y}} + \bar{w}\frac{\partial \bar{v}}{\partial \bar{z}}\right) = -Re\frac{\partial \bar{p}}{\partial \bar{y}} + \left(\frac{\partial^2 \bar{v}}{\partial \bar{x}^2} + \frac{\partial^2 \bar{v}}{\partial \bar{y}^2}\right), \tag{8}$$

$$Re\left(\bar{u}\frac{\partial \bar{u}}{\partial \bar{x}} + \bar{v}\frac{\partial \bar{u}}{\partial \bar{y}} + \bar{w}\frac{\partial \bar{u}}{\partial \bar{z}}\right) = -Re\frac{\partial \bar{p}}{\partial \bar{x}} + \left(\frac{\partial^2 \bar{u}}{\partial \bar{x}^2} + \frac{\partial^2 \bar{u}}{\partial \bar{y}^2}\right), \tag{9}$$

$$Re\left(\bar{u}\frac{\partial \bar{w}}{\partial \bar{x}} + \bar{v}\frac{\partial \bar{w}}{\partial \bar{y}} + \bar{w}\frac{\partial \bar{w}}{\partial \bar{z}}\right) = -f(\bar{z}) + \left(\frac{\partial^2 \bar{w}}{\partial \bar{x}^2} + \frac{\partial^2 \bar{w}}{\partial \bar{y}^2}\right), \tag{10}$$

$$R_e S_{Ck}\left(\bar{u}\frac{\partial X_k}{\partial \bar{x}} + \bar{v}\frac{\partial X_k}{\partial \bar{y}} + \bar{w}\frac{\partial X_k}{\partial \bar{z}}\right) = \left(\frac{\partial^2 X_k}{\partial \bar{x}^2} + \frac{\partial^2 X_k}{\partial \bar{y}^2}\right), \tag{11}$$

where S_{Ck} is the Schmidt number for species kth component, and $f(\bar{z}) = (1/Re)(\partial \bar{p}/\partial \bar{z})$.

2.2. In the gas diffusers

The gas diffusers are made from graphite cloth, which can be modeled as porous media. In porous media, the Navier–Stokes equations are still valid but only for each fluid element inside the micro channel. However, due to

the complex geometric configuration, the flow becomes very complicated and some kind of averaging is necessary to make the problem more tractable mathematically. This idea is in some way similar to the time-averaging approach in turbulent flow. In porous media instead, a volume averaging process is performed. So the macroscopic velocity field in the gas diffuser is provided by the expression obtained by the volume-averaged Navier–Stokes equations. The resulting equations are a generalized form of Darcy's law [25] and in dimensionless form as:

$$\frac{\partial \bar{u}}{\partial \bar{x}}+\frac{\partial \bar{v}}{\partial \bar{y}}+\frac{\partial \bar{w}}{\partial \bar{z}}=0, \tag{12}$$

$$Re\,\frac{1}{\varepsilon^2}\left(\bar{u}\frac{\partial \bar{u}}{\partial \bar{x}}+\bar{v}\frac{\partial \bar{u}}{\partial \bar{y}}+\bar{w}\frac{\partial \bar{u}}{\partial \bar{z}}\right) = -Re\,\frac{\partial \bar{p}}{\partial \bar{x}}+\frac{1}{\varepsilon}\left(\frac{\partial^2 \bar{u}}{\partial \bar{x}^2}+\frac{\partial^2 \bar{u}}{\partial \bar{y}^2}\right)-\frac{1}{\bar{\kappa}}\bar{u}, \tag{13}$$

$$Re\,\frac{1}{\varepsilon^2}\left(\bar{u}\frac{\partial \bar{v}}{\partial \bar{x}}+\bar{v}\frac{\partial \bar{v}}{\partial \bar{y}}+\bar{w}\frac{\partial \bar{v}}{\partial \bar{z}}\right) = -Re\,\frac{\partial \bar{p}}{\partial \bar{y}}+\frac{1}{\varepsilon}\left(\frac{\partial^2 \bar{v}}{\partial \bar{x}^2}+\frac{\partial^2 \bar{v}}{\partial \bar{y}^2}\right)-\frac{1}{\bar{\kappa}}\bar{v}, \tag{14}$$

$$Re\,\frac{1}{\varepsilon^2}\left(\bar{u}\frac{\partial \bar{w}}{\partial \bar{x}}+\bar{v}\frac{\partial \bar{w}}{\partial \bar{y}}+\bar{w}\frac{\partial \bar{w}}{\partial \bar{z}}\right) = -f(\bar{z})+\frac{1}{\varepsilon}\left(\frac{\partial^2 \bar{w}}{\partial \bar{x}^2}+\frac{\partial^2 \bar{w}}{\partial \bar{y}^2}\right)-\frac{1}{\bar{\kappa}}\bar{w}, \tag{15}$$

$$R_e S_{Ck}\,\frac{1}{\varepsilon^2}\left(\bar{u}\frac{\partial X_k}{\partial \bar{x}}+\bar{v}\frac{\partial X_k}{\partial \bar{y}}+\bar{w}\frac{\partial X_k}{\partial \bar{z}}\right)=\left(\frac{\partial^2 X_k}{\partial \bar{x}^2}+\frac{\partial^2 X_k}{\partial \bar{y}^2}\right). \tag{16}$$

The Schmidt number is defined in terms of the effective macroscopic diffusion coefficient [14]:

$$S_{Ck}=\frac{\mu}{\rho D_{\mathrm{eff},k}}, \tag{17}$$

where

$$D_{\mathrm{eff},k}=\frac{3\varepsilon-1}{2\varepsilon}D_k. \tag{18}$$

2.3. In the catalyst layers

Oxygen or hydrogen enters the gas channel, passes through the porous gas diffuser and then reaches the catalyst layer. Three species, which are electrons, protons, and oxygen or hydrogen molecules, must meet at the surface of the catalyst layer. The catalyst layer consists of three different substances: catalyst particles, solid polymer, and a porous carbon cloth. The solid polymer provides pathways for the protons whereas carbon cloth allows electrons and oxygen or hydrogen to reach the catalyst sites along the carbon threads and through the pores, respectively. The motions of electrons in the carbon phase and ions in the membrane are governed by their own potentials. The difference between these potentials drives the electrochemical reaction. The rate of electrochemical reaction, which converts ionic current into electronic current, is expressed by the relationship between the concentration of reactant and the potential drop across the electrolyte interface. We adopt Butler–Volmer expressions as follows [14]:

$$j_{\mathrm{a}}=a j_{0,\mathrm{a}}^{\mathrm{ref}}\left(\frac{X_{\mathrm{H_2}}}{X_{\mathrm{H_2}}^{\mathrm{ref}}}\right)^{1/2}\left[\mathrm{e}^{(\alpha_{\mathrm{a}}F/RT)\eta}-\frac{1}{\mathrm{e}^{(\alpha_{\mathrm{c}}F/RT)\eta}}\right], \tag{19}$$

$$j_{\mathrm{c}}=a j_{0,\mathrm{c}}^{\mathrm{ref}}\left(\frac{X_{\mathrm{O_2}}}{X_{\mathrm{O_2}}^{\mathrm{ref}}}\right)\left[\mathrm{e}^{(\alpha_{\mathrm{a}}F/RT)\eta}-\frac{1}{\mathrm{e}^{(\alpha_{\mathrm{c}}F/RT)\eta}}\right], \tag{20}$$

where η is the over-potential, defined as $\eta=E^{\mathrm{o}}-\Phi$ where E^{o} is the open circuit potential, which is a function of the temperature. E^{o} is defined in the following Eq. [26]:

$$E^{\mathrm{o}}=0.0025T+0.2329. \tag{21}$$

The governing equations for catalyst layer are as follows:

$$Re\,\frac{1}{\varepsilon_{\mathrm{c}}^2}\left(\bar{u}\frac{\partial \bar{u}}{\partial \bar{x}}+\bar{v}\frac{\partial \bar{u}}{\partial \bar{y}}+\bar{w}\frac{\partial \bar{u}}{\partial \bar{z}}\right) = -Re\,\frac{\partial \bar{p}}{\partial \bar{x}}+\frac{1}{\varepsilon_{\mathrm{c}}}\left(\frac{\partial^2 \bar{u}}{\partial \bar{x}^2}+\frac{\partial^2 \bar{u}}{\partial \bar{y}^2}\right)-\frac{1}{\bar{\kappa}}\bar{u}+\frac{k_\Phi}{k_{\mathrm{p}}}z_{\mathrm{f}}c_{\mathrm{f}}F \times\frac{\partial \Phi}{\partial \bar{x}}\frac{Re\,D_{\mathrm{e}}}{\varepsilon_{\mathrm{c}}}, \tag{22}$$

$$Re\,\frac{1}{\varepsilon_{\mathrm{c}}^2}\left(\bar{u}\frac{\partial \bar{v}}{\partial \bar{x}}+\bar{v}\frac{\partial \bar{v}}{\partial \bar{y}}+\bar{w}\frac{\partial \bar{v}}{\partial \bar{z}}\right) = -Re\,\frac{\partial \bar{p}}{\partial \bar{y}}+\frac{1}{\varepsilon_{\mathrm{c}}}\left(\frac{\partial^2 \bar{v}}{\partial \bar{x}^2}+\frac{\partial^2 \bar{v}}{\partial \bar{y}^2}\right)-\frac{1}{\bar{\kappa}}\bar{v}+\frac{k_\Phi}{k_{\mathrm{p}}}z_{\mathrm{f}}c_{\mathrm{f}}F \times\frac{\partial \Phi}{\partial \bar{y}}\frac{Re\,De}{\varepsilon_{\mathrm{c}}}, \tag{23}$$

$$Re\,\frac{1}{\varepsilon_{\mathrm{c}}^2}\left(\bar{u}\frac{\partial \bar{w}}{\partial \bar{x}}+\bar{v}\frac{\partial \bar{w}}{\partial \bar{y}}+\bar{w}\frac{\partial \bar{w}}{\partial \bar{z}}\right) = -f(\bar{z})+\frac{1}{\varepsilon_{\mathrm{c}}}\left(\frac{\partial^2 \bar{w}}{\partial \bar{x}^2}+\frac{\partial^2 \bar{w}}{\partial \bar{y}^2}\right)-\frac{1}{\bar{\kappa}}\bar{w}+\frac{k_\Phi}{k_{\mathrm{p}}}z_{\mathrm{f}}c_{\mathrm{f}}F \times\frac{\partial \Phi}{\partial \bar{z}}\frac{ReD_{\mathrm{e}}}{\varepsilon_{\mathrm{c}}}, \tag{24}$$

$$R_e S_{Ck}\,\frac{1}{\varepsilon_{\mathrm{c}}^2}\left(\bar{u}\frac{\partial X_k}{\partial \bar{x}}+\bar{v}\frac{\partial X_k}{\partial \bar{y}}+\bar{w}\frac{\partial X_k}{\partial \bar{z}}\right)=\left(\frac{\partial^2 X_k}{\partial \bar{x}^2}+\frac{\partial^2 X_k}{\partial \bar{y}^2}\right)+S_k, \tag{25}$$

where $\varepsilon_c = \varepsilon_m \varepsilon_{mc}$, ε_m is the membrane porosity, ε_{mc} is the membrane volume fraction, and S_k is the source term. For hydrogen in anode catalyst layer

$$S_k = -\frac{1}{2F} j_a \frac{\rho D_e^2}{\mu c_{tota}}$$

for oxygen in cathode catalyst layer

$$S_k = -\frac{1}{4F} j_c \frac{\rho D_e^2}{\mu c_{totc}}$$

and for H_2O,

$$S_k = -\frac{1}{2F} j_c \frac{\rho D_e^2}{\mu c_{totc}}.$$

The phase potential equation can be obtained from:

$$\nabla(\sigma_m \nabla \Phi) + S_\Phi = 0, \tag{26}$$

where S_Φ is the source term that equals j_a for anode catalyst layer or j_c for cathode catalyst layer. Here σ_m is the proton conductivity in the membrane phase, which can be correlated by Springer et al. [27] as:

$$\sigma_m = \exp\left(1268\left(\frac{1}{303} - \frac{1}{T}\right)\right)(0.005139\lambda - 0.00326). \tag{27}$$

The water content λ, in Eq. (27) can be expressed as follows [25]:

$$\begin{aligned} &\lambda = 0.043 + 17.81a - 39.85a^2 + 36a^3 && \text{for } 0 < a < 1, \\ &\lambda = 14 + 1.4(a-1) && 1 \leqslant a \leqslant 3. \end{aligned} \tag{28}$$

Note that a is defined as the vapor activity at the cathode gas diffuser catalyst layers interface assuming thermodynamic equilibrium, which is given by

$$a = \frac{X_w p}{p^{sat}}. \tag{29}$$

The saturated water partial pressure, p^{sat} is expressed by the following empirical equation:

$$\log_{10} p^{sat} = -2.1794 + 0.2953T - 9.1837 \times 10^{-5} T^2 + 1.4454 \times 10^{-7} T^3. \tag{30}$$

2.4. In the membrane

Momentum equations in porous membrane are related to water transportation. The governing equations are similar as those in catalyst layer (Eqs. (22)–(24)) except porosity is different.

Inside the membrane there is no chemical reaction, hence the phase potential equation is as follows:

$$\nabla(\sigma_m \nabla \Phi) = 0. \tag{31}$$

3. Boundary conditions

Boundary conditions at the gas channel entries, such as gas mixture velocities, pressure, and component concentrations, are specified. No slip boundary conditions are specified at the gas channel walls. At the interface between the gas channel and electron collectors, the boundary conditions of components concentration are assumed as:

$$\frac{\partial X_i}{\partial n} = 0. \tag{32}$$

For the membrane potential equations, the boundary conditions are:

$$\frac{\partial \Phi}{\partial \bar{y}} = \frac{\partial \Phi}{\partial \bar{z}} = 0. \tag{33}$$

This means that no proton current leaves upper, lower, entrance and exit limits. In x-direction,

$$\Phi|_{\bar{x}=0} = 0, \qquad \left.\frac{\partial \Phi}{\partial \bar{x}}\right|_{\bar{x}=L} = 0. \tag{34}$$

No boundary conditions are needed at the interface between gas channel and gas diffuser because they are coupled.

4. Numerical modeling

4.1. Numerical analysis

The fluid flow phenomenon has two main parts that are strongly interdependent. One is fluid flow governed by Navier–Stokes equations, and the other is species transportation governed by electrochemical reactions. In the cathode channel, chemical reaction product, H_2O, is produced on the surface of the catalyst layer. It diffuses to the entire gas channel from the interface between gas diffuser and catalyst layer.

The velocity and pressure fields for the gas mixtures are solved first in the coupled gas channel, gas diffuser and catalyst layer domain. The composition of the gas will change along with the chemical reaction, but the gas mixture properties are treated as constant such as gas constant, density and so on. After the velocity and pressure distribution calculated, the species concentration equations can be solved in the combined single domain of both anode and cathode channels, which depends on the transfer current density.

4.2. Vorticity–velocity method for 3-D parabolic flow with power-law scheme

A vorticity–velocity method successfully developed for two-dimensional flow by Farouk and Fusegi [28].

This method can be extended directly to a three-dimensional parabolic flow as shown in Chou and Hwang [29] and Jen and Lavine [30], and will be used in the present study.

The axial vorticity function is defined as:

$$\zeta = \frac{\partial \bar{u}}{\partial \bar{y}} - \frac{\partial \bar{v}}{\partial \bar{x}}. \tag{35}$$

Applying it to continuity equation:

$$\nabla^2 \bar{u} = \frac{\partial \zeta}{\partial \bar{y}} - \frac{\partial^2 \bar{w}}{\partial \bar{x} \partial \bar{z}}, \tag{36}$$

$$\nabla^2 \bar{v} = -\frac{\partial \zeta}{\partial \bar{x}} - \frac{\partial^2 \bar{w}}{\partial \bar{y} \partial \bar{z}}. \tag{37}$$

Cross differentiation of x and y momentum equations of gas channel eliminate pressure terms yield:

$$\bar{u}\frac{\partial \zeta}{\partial \bar{x}} + \bar{v}\frac{\partial \zeta}{\partial \bar{y}} + \bar{w}\frac{\partial \zeta}{\partial \bar{z}} + \zeta\left(\frac{\partial \bar{u}}{\partial \bar{x}} + \frac{\partial \bar{v}}{\partial \bar{y}}\right) + \left(\frac{\partial \bar{w}}{\partial \bar{y}}\frac{\partial \bar{u}}{\partial \bar{z}} - \frac{\partial \bar{w}}{\partial \bar{x}}\frac{\partial \bar{v}}{\partial \bar{z}}\right) = \frac{1}{Re}\left(\frac{\partial^2 \zeta}{\partial \bar{x}^2} + \frac{\partial^2 \zeta}{\partial \bar{y}^2}\right). \tag{38}$$

Using the same method we can get similar equation of gas diffuser

$$Re\,\frac{1}{\varepsilon}\left(\bar{u}\frac{\partial \zeta}{\partial \bar{x}} + \bar{v}\frac{\partial \zeta}{\partial \bar{y}} + \bar{w}\frac{\partial \zeta}{\partial \bar{z}} + \zeta\left(\frac{\partial \bar{u}}{\partial \bar{x}} + \frac{\partial \bar{v}}{\partial \bar{y}}\right) + \left(\frac{\partial \bar{w}}{\partial \bar{y}}\frac{\partial \bar{u}}{\partial \bar{z}} - \frac{\partial \bar{w}}{\partial \bar{x}}\frac{\partial \bar{v}}{\partial \bar{z}}\right)\right) + \frac{\varepsilon}{\bar{\kappa}}\zeta = \left(\frac{\partial^2 \zeta}{\partial \bar{x}^2} + \frac{\partial^2 \zeta}{\partial \bar{y}^2}\right). \tag{39}$$

An additional constraint, which will be used to determine $f(\bar{z})$, is that global mass conservation must be satisfied as follows:

$$\int\int \bar{w}\,\mathrm{d}\bar{x}\,\mathrm{d}\bar{y} = \frac{(1+r)^2}{4r}, \tag{40}$$

where $r = a/b$ is the aspect ratio of the gas channel.

4.3. Discretization strategies

In order to solve the above equations, some terms need to be discretized furthermore. The strategies of discretization is as follows:

The values of $\partial \bar{w}/\partial \bar{x}$, $\partial \bar{w}/\partial \bar{y}$, $\partial \bar{u}/\partial \bar{x}$ and $\partial \bar{v}/\partial \bar{y}$ are discretized using central differencing at each grid point. The values of $\partial \bar{u}/\partial \bar{z}$ and $\partial \bar{v}/\partial \bar{z}$, $\partial \Phi/\partial \bar{z}$ are computed by two points backward differencing. The values of $\partial^2 \bar{w}/\partial \bar{x}\partial \bar{z}$, $\partial^2 \bar{w}/\partial \bar{y}\partial \bar{z}$, $\partial \zeta/\partial \bar{x}$ and $\partial \zeta/\partial \bar{y}$ are calculated by using backward differences axially and central differences in the transverse directions.

The values of vorticity on the boundary can be evaluated as shown in Fig. 2.

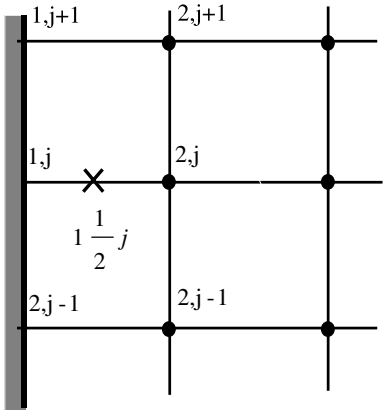

Fig. 2. Vorticity at the wall.

$$\varsigma_{1\frac{1}{2},j} = \frac{1}{2}(\varsigma_{1,j} + \varsigma_{2,j}) = \frac{1}{2\Delta y}(u_{1\frac{1}{2},j+1} - u_{1\frac{1}{2},j-1}) - \frac{v_{2,j}}{\Delta x}, \tag{41}$$

$$u_{1\frac{1}{2},j+1} = \tfrac{1}{2}u_{2,j+1}, \qquad u_{1\frac{1}{2},j-1} = \tfrac{1}{2}u_{2,j-1}, \tag{42}$$

$$\varsigma_{1,j} = -2v_{2,j}/\Delta x + (u_{2,j+1} - u_{2,j-1})/(2\Delta y) - \varsigma_{2,j}. \tag{43}$$

4.4. Solution algorithms

1. Solve velocity and pressure field for anode domain first. The initial values of the unknown, $\bar{u}$, $\bar{v}$ and ζ are assigned to be zero at the entrance, $\bar{z} = 0$. Uniform inlet axial velocity (i.e. $\bar{w} = 1$) is used. Note that $\zeta = 0$ at $\bar{z} = 0$ results from the vorticity definition.
2. Discretizing Eqs. (38) and (39) with power-law scheme [24] and solving them in the coupled domain, one can get vorticity ζ for gas channel, gas diffuser and catalyst layer.
3. The elliptic-type equations (36) and (37) are solved for and iteratively. During the iteration process, the values of vorticity on the boundaries are evaluated using Eq. (43).
4. Using control volume method with power-law scheme to discretize equation (10), (15) and (24), plug in new value $\bar{u}$ and $\bar{v}$ solved in above step 2, one can solve axial velocity in coupled domain with constraint (40) to meet the requirement of the constraint flow rate.
5. Steps 3–4 are repeated at a cross-section until the following convergence criterion is satisfied for the velocity components $\bar{u}$ and $\bar{v}$:

$$\frac{\max|\bar{u}_{i,j}^{n+1} - \bar{u}_{i,j}^{n}|}{\max|\bar{u}_{i,j}^{n+1}|} < 10^{-5}, \tag{44}$$

   where n is the nth iteration of steps 3–4.
6. Repeat steps 1–5 for cathode domain. One can get velocity distribution for gas channels, gas diffusers and catalyst layers in cathode domain.

7. With obtained solutions, $\bar{u}$, $\bar{v}$ and $\bar{w}$ for both anode and cathode electrolytes, species concentration equations and potential equations for a single domain from anode electrolyte to cathode electrolyte can be solved iteratively. These steps are repeated until the following convergence criterion is satisfied:

$$\max\left(\frac{\max|X_k^{m+1}|-X_k^m}{\max|X_k^{m+1}|},\frac{\Phi^{m+1}=\Phi^m}{\Phi^{m+1}}\right)<10^{-6}, \quad (45)$$

where m is the mth iteration of step 6, and k is the kth species.

8. Steps 3–7 are repeated at the next axial location until the final z location is reached.
9. Once the electrolyte phase potential is obtained, the local current density can be calculated along the axial direction using following equation:

$$I(\bar{z})=-\sigma_m\frac{\partial\Phi}{\partial x}. \quad (46)$$

The average current density is then determined by

$$I_{avg}=\frac{1}{L}\int_0^L I(\bar{z})\,d\bar{z}. \quad (47)$$

5. Computational tests and details

A uniform mesh size of 41×201 is used for the cross-section in anode domain and cathode domain respectively (Table 2). The axial step size Δz was varied from 10^{-5} near the channel entrance to about 2.5×10^{-3} near the fully developed region. The grid independence test in the cross-section and axial direction have been performed for denser grid (61×301) and $\Delta z=10^{-6}$. The changes in predicted friction coefficient is less than 1% at the same flow condition. As additional verification of the computational procedure, the hydrodynamically developing flow was calculated without porous media (let porosity equals 1 and permeability equals a very large number). The results were compared with Shah and London [31] and Curr et al. [32]. The apparent friction factors were found to agree within 2% at all axial stations.

6. Results and discussion

In the present calculation, the channel aspect ratio is chosen to be at 0.2 and $Re=17$. Note that this is a typical PEM fuel cell gas channel's geometry and inlet flow condition, which is adopted from Bernadi and Verbrugge [11]. The physical properties and parameters of the present study are listed in Table 1.

Table 1
Physical parameters, properties and operation conditions

Gas channel length	7.67 cm
Gas channel width	0.0762 cm
Gas channel height	0.5 cm
Gas diffuser width	0.0254 cm
Catalyst layer width	0.00287 cm
Membrane width	0.023 cm
Gas diffuser porosity, ε	0.4
Membrane porosity, ε_m	0.28
Volume fraction membrane in catalyst layer, ε_{mc}	0.5
Permeability of the gas diffuser, κ	1.76×10^{-7} cm^2
Hydraulic permeability of membrane, κ_p	1.8×10^{-14} cm^2
Electro kinetic permeability, κ_ϕ	7.18×10^{-16} cm^2
Universal gas constant, R	8.314 J/mol K
Faraday constant, F	96487 C/mol
Fixed site charge, z_f	−1
Anode transfer coefficient, α_a	2
Cathode transfer coefficient, α_c	2
Reference exchange current density times area of anode, $aj_{0,a}^{ref}$	5×10^2 A/cm^3
Reference exchange current density times area of cathode, $aj_{0,c}^{ref}$	1×10^{-4}A/cm^3
Oxygen reference concentration	3.39×10^{-6} mol/cm^3
Hydrogen reference concentration	5.64×10^{-5} mol/cm^3
Total mole concentration at the anode side, c_{tota}	66.817mol/cm^3
Total mole concentration at the cathode side, c_{totc}	1.7808×10^{-5} mol/cm^3
Inlet velocity	35 cm/s

6.1. Development of axial velocity profiles

Due to the similar velocity profiles in both anode channel and cathode channel, only the velocity profiles in the cathode channel will be displayed in this paper.

The developing profiles of the axial velocity along the centerline $\bar{y}=1.5$, are illustrated in Fig. 3. The axial velocity at different locations, $\bar{z}=0.0002$, 0.0005, 0.0008, 0.003, 0.02, and 0.2 are plotted for the gas channel and gas diffuser. It is well known that the axial velocity profiles for a rectangular channel are symmetric about the center axis in both y and x directions. However, due to the effects of the gas diffuser, which consists of porous media, the shift of velocity profiles become apparent. As shown in Fig. 3(a), the velocity profiles are plotted starting from very close to the entrance ($\bar{z}=0.0002$) to a fully developed location ($\bar{z}=0.2$). Near the entrance region, the axial velocity profile in gas channel is fairly uniform, at $\bar{z}=0.0002$. The axial velocity in gas channel reaches maximum value at about $\bar{z}=0.02$, and the flow is very close to fully developed. Clearly the axial velocity profiles are parabolic at fully developed regions. However, it is worth pointing out that the maximum velocity does not locate on the

Table 2
Computational test

Grids	31×151	41×201	61×301
$Z = 0.0008$			
w at $x = 0.2$, $y = 0.2$	1.644448	1.642347	1.639776
w at $x = 0.9$, $y = 0.9$	0.039596	0.039425	0.039173
Number of cells	0	0	0
$Z = 0.002$			
w at $x = 0.2$, $y = 0.2$	1.842195	1.807892	1.806438
w at $x = 0.2$, $y = 0.2$	0.0041162	0.0040582	0.0040491
Number of cells	4	4	4

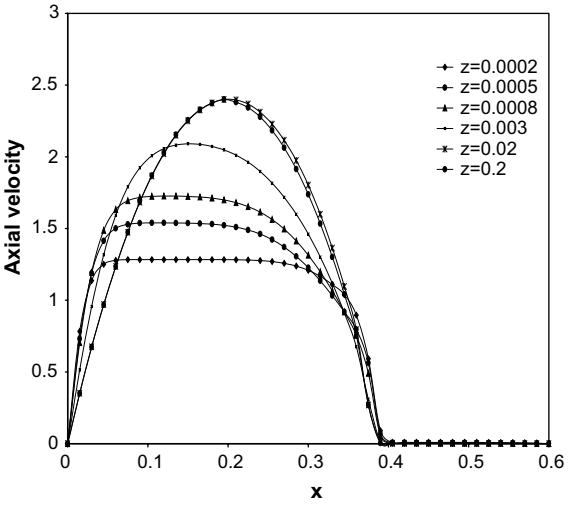

Fig. 3. Axial velocity.

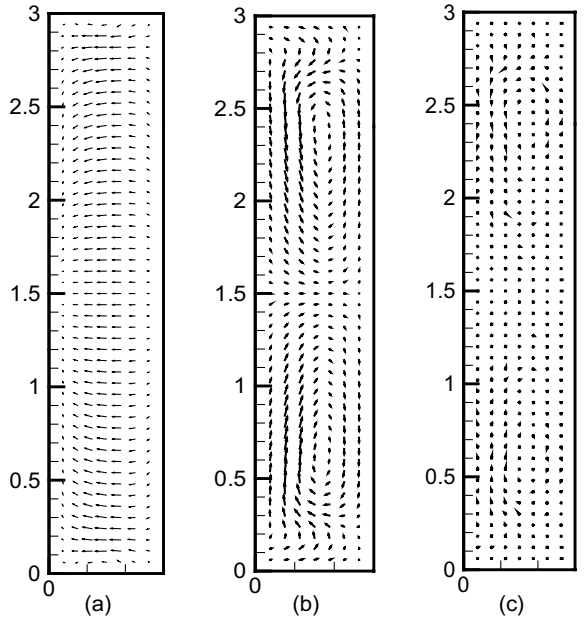

Fig. 4. Secondary flow vector plots at: (a) $\bar{z} = 0.0005$, (b) $\bar{z} = 0.008$ and (c) $\bar{z} = 0.2$.

centerline between the wall and the interface of the gas channel and gas diffuser. Instead, the maximum velocity shifts slightly to the gas diffuser side because the velocity on the interface of the gas diffuser and gas channel is not zero (i.e., slip plus slaving boundary conditions) due to porous layer [23].

6.2. Secondary flow patterns

Fig. 4(a)–(c) show secondary flow plots for three different axial locations, at $\bar{z} = 0.0005$, 0.008 and 0.2, respectively. At the location $\bar{z} = 0.0005$, as shown in Fig. 4(a), the secondary flow moves out form porous media in the core region. This is simply due to the acceleration of the core gas channel flow in the early entrance region. Fig. 4(b) shows the vector secondary flow pattern at $\bar{z} = 0.008$, which has two pairs of vortices, with one small pair counter rotating cells near the corner of the gas channel. It is observed that, near the core region, a fairly uniform secondary flow running from the left side to right side into the gas diffuser, and there are outflows from the gas diffuser to gas channel near the top and bottom wall. It is also interesting to see two counter rotating cells at the top and bottom left corner, which are generated due to the corner effect of the gas channel. In nearly fully developed region at $\bar{z} = 0.2$, the secondary flow strength has decreased significantly, and the effect of cross-sectional convection is negligible.

6.3. Cell potential and current density

The discussion of the results is divided into two sections. In the first section, the model results are analyzed and discussed in light of corresponding experimental investigation from the literature. In the second section, the membrane properties and cell operational condition are varied to investigate the changes in cell polarization

characteristics. All the following current density profiles are the average results at the whole reaction channel.

6.4. Comparison of model results and experimental investigations

Fig. 5 compares the calculated single fuel-cell potential as a function of current density with the experimental results published by Ticianelli et al. [12,13] with the condition corresponding to the polymer-electrolyte, 20 wt. Pt, 50-nm Pt sputter, 5 atm cathode pressure, 3 atm anode pressure. The cell temperatures are at 353 and 323 K in Fig. 5(a) and (b), respectively. The calculated curves show very good agreements with the experimental data for both temperatures. As shown in these figures, at low current densities, the potential drops quickly due to activation overpotential of oxygen reduction reaction; and at high current densities, the potential drops almost linearly with increasing current density due to the greater influence of potential drop through the membrane.

As seen from the figures, a slight deviation of the model results in comparison to experimental data. This may be due to slight error in the data manually extracted the experimental data from Ticianelli et al. [12,13]. Another possibility is thermodynamic open circuit potential errors. In this model, the empirical open circuit potential results of Parthasarathy et al. [26] are used. They tabulated values for the open circuit potential as a function of temperature, which is $V_{oc} = 0.0025T + 0.2329$.

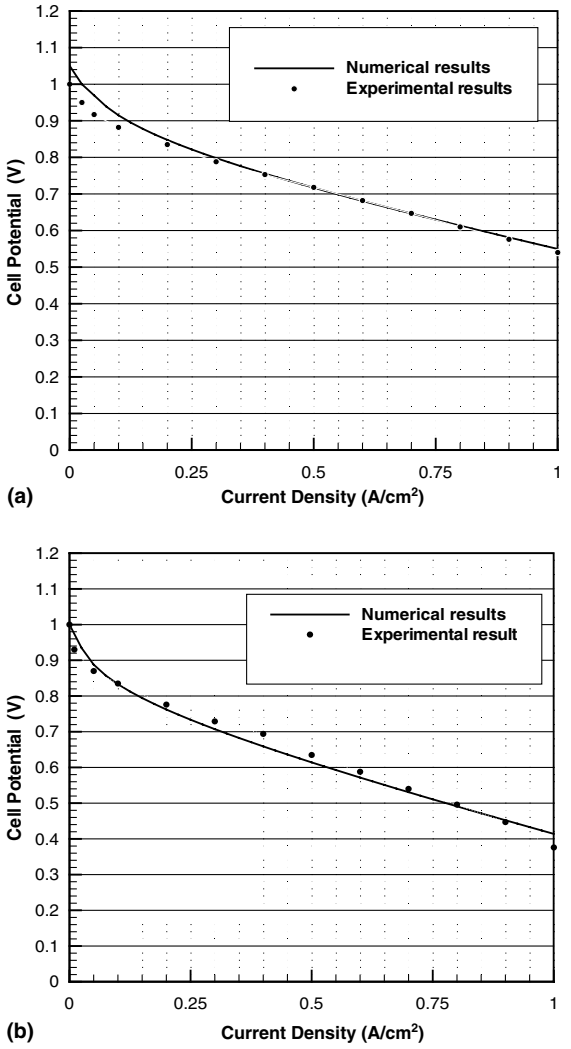

Fig. 5. Numerical results vs. experimental data of Ticianelli [12,13] at: (a) $T = 353$ K and (b) $T = 323$ K.

6.5. Effects of membrane thickness and cell operational parameters

6.5.1. Effects of membrane thickness

In Fig. 6, we investigate the effects of membrane thickness on the fuel-cell potential and current density. As we know, ion conductivity resistance decreases as the membrane thickness decreases and it has no effect on the cell open circuit potential. In order to compare our model results with the experimental data published by Bernardi and Verbrugge [33], the cell temperature and pressure are set to be at 368 K and 4 atm respectively, as inputs to our numerical model. The membrane thickness decreases from 0.01061 to 0.00508 cm, which are equivalent to 4–2 mil in Bernardi's original results.

It can be seen from Fig. 6 that fuel cell potential clearly increases as decreasing membrane thickness. The agreement between our prediction results and experimental results is generally satisfactory.

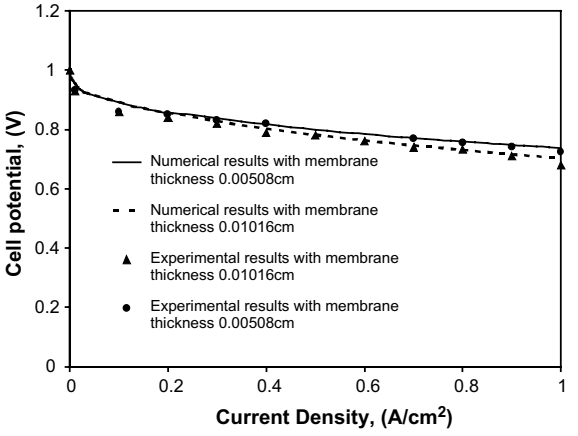

Fig. 6. Effects of membrane thickness.

6.5.2. Effects of differential pressure and temperature

Fig. 7(a) shows the effect of pressure variations on the PEM fuel cell potential and current density. When the cathode pressure increases from 3 to 5 atm at 353K, the gas density and concentration increase, which causes more oxygen molecules involved in chemical reactions. Ticianelli et al. [12] plotted the cell potential as a function of pressure with a constant current density. In their experimental results, a plot of the cell potential vs. $\log(P_{O_2})$ for four different current densities are presented. Using this numerical model, our predictions agree very well with their experimental data (not shown).

The anode and cathode gas bulk temperatures are nearly maintained at a constant value in the fuel cell. Four different temperatures on fuel cell performance are plotted in Fig. 7(b) at a constant pressure 3 atm. It is observed that when the bulk temperature increases, the cell potential increases. Physically, when the gas stream temperature increases, the reactants electrochemical kinetic energy increases; thus increases the oxygen reduction reaction further. This causes an increase in water vapor concentration at the cathode gas-diffuser catalyst layer interface, which increases the transport capability of the membrane, and the ion conductivity resistance is decreased. As a result, the slope of the linear region in the cell potential vs. current density plot is also decreased. When the temperature is increased, the fall-off in cell potential is decreased at higher current density. It can be found that the bulk temperature not only affects cell performance potential, but it also affects cell open circuit potential.

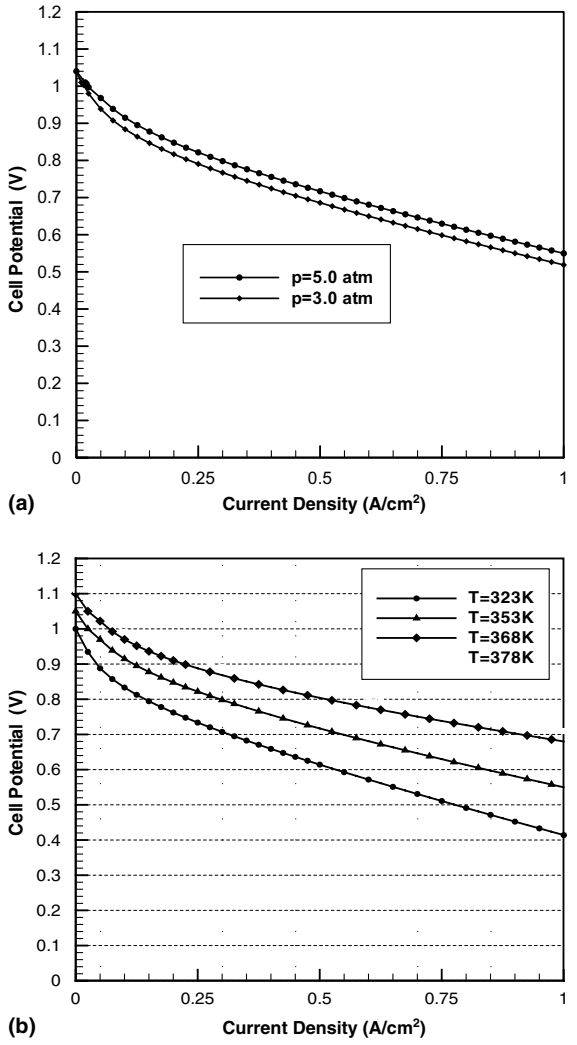

Fig. 7. The effects of temperature and pressure on the performance of fuel cell at: (a) $T = 353$ K and (b) $p = 5$ atm.

6.5.3. Oxygen and hydrogen mole fraction in gas channels and gas diffusers

Fig. 8(a)–(d) show the oxygen and hydrogen mole fraction contour plots in the coupled gas channel and gas diffuser in the anode and cathode, respectively, at two different locations (i.e, at $\bar{z} = 0.008$ and $\bar{z} = 0.2$). It can be seen from the figure that the mole fraction are obviously different at these two locations. At the location $\bar{z} = 0.008$, the oxygen and hydrogen mole fraction patterns have nearly the similar curves with different magnitude. This can be explained by the secondary flow convective effect from Fig. 4(b). Near the core region, the secondary flow is flowing uniformly toward the gas diffuser, as shown in Fig. 4(b), so fairly compressed and flat concentration distributions (for both oxygen and hydrogen) are observed. Near the top and bottom walls, the secondary flow flows from gas diffuser to gas channel (i.e., from left to right), thus we can see higher concentrations near the top and bottom walls. The small bumps of the concentration distributions are due to the existence of the two counter rotating cells at the corner of the gas channel (see Fig. 4(b)). In the fully developed region, i.e. $\bar{z} = 0.2$, however, since the secondary flow strength is very weak, the convective terms in the cross-sectional direction (x and y) are very small, therefore, diffusion components dominate the flow pattern, the contributions of the convective portions in species transport equations are essentially negligible. Thus, the mole fraction patterns for both oxygen and hydrogen appear to be very uniform. Along the axial direction both the oxygen and the hydrogen mole fraction decrease, as displayed in Fig. 8(c) and (d), due to electrochemical reaction consumes both fuel and oxidizer. However, the hydrogen consumption is much higher than the oxygen consumption. In the present model, it is assumed that liquid water only exits in the membrane. However, if the electrochemical reaction rate is sufficiently high, the amount of water produced is condensed into liquid state in gas channel. In this case, a two-phase

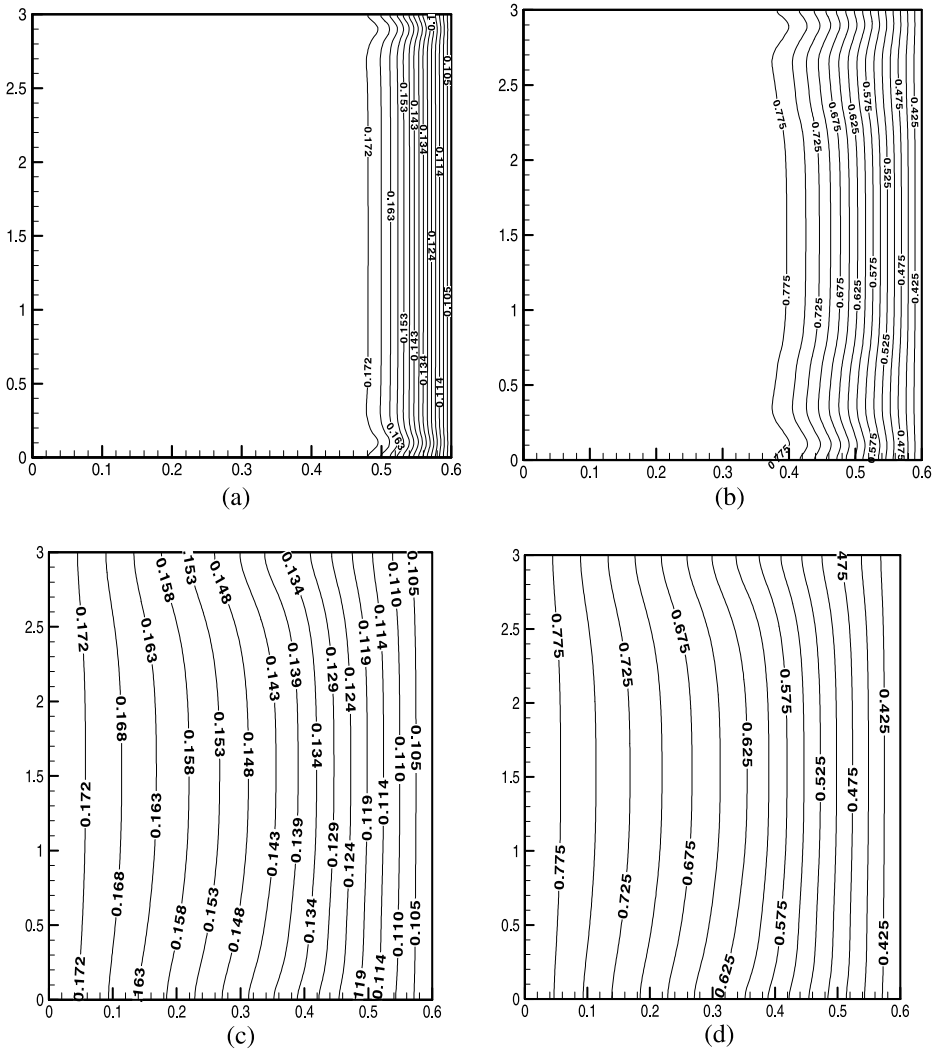

Fig. 8. Concentration contour plots for hydrogen and oxygen: (a) oxygen mole fraction at $\bar{z} = 0.008$, (b) hydrogen mole fraction at $\bar{z} = 0.008$, (c) oxygen mole fraction at $\bar{z} = 0.2$ and (d) hydrogen mole fraction at $\bar{z} = 0.2$.

flow model needs to be developed. However, this is beyond the scope of the present study.

7. Conclusion

A three-dimensional theoretical model is presented here to enable the prediction of the flow and mass concentration patterns in the entire fuel cell channels including the gas channel and gas diffuser. Those flow and concentration properties include axial velocity distributions in the semi-porous channel, polarization curves, and reactant concentration distributions along the axial direction of the fuel cell are investigated in details. The electrochemical kinetics, current density distribution, hydrodynamics, and multi-component transport in the fuel cell, which affect the performance of a PEM fuel cell, are studied and demonstrated in this paper. In the numerical analysis, a vorticity–velocity with power-law scheme method was successfully adapted to simulate multi-dimensional flow and mass concentration distributions in the fuel cell. It is also found that the simulated data compare well with the published experimental results.

References

[1] B.J. Crowe, Fuel cells: A Survey, NASA Rep. (SP-5115), Washington, DC, 1973.
[2] K.B. Prater, Power sources 51 (1994) 129–144.
[3] S. Gottesfeld, in: C. Tobias (Ed.), Advances in Electrochemical Science and Engineering, vol. 5, John Wiley & Sons, New York, 1997, pp. 195–301.

[4] R.F. Savinell, S.D. Fritts, Theoretical performance of a hydrogen-bromine rechargeable SPE fuel cell, J. Power Sources 22 (1988) 423.
[5] S.J. Ridge, R.E. White, Y. Tsau, R.N. Beaver, G.A. Eisman, Oxygen reduction in a proton exchange membrane test cell, J. Electrochem. Soc. 136 (1989) 1902.
[6] S.D. Fritts, R.F Savinell, Simulation studies on the performance of the hydrogen electrode bonded to proton exchange membranes in the H_2–Br_2 fuel cell, J. Power Source 28 (1990) 301–315.
[7] S.C. Yang, M.B. Cutlip, P. Stonehart, Further development of an approximate model for mass transfer with reaction in porous gas-diffusion electrodes to include substrate effects, Electrochim. Acta 34 (1989) 703.
[8] M.W. Verbrugge, R.F. Hill, Ion and solvent transport in ion-exchange membranes, J. Electrochem. Soc. 137 (1990) 886.
[9] M.W. Verbrugge, R.F. Hill, Transport phenomena in perfluorosulfonic acid membranes during the passage of current, J. Electrochem. Soc. 137 (1990) 1131.
[10] N. Giordano, E. Passalacqua, V. Aiderucci, P. Staiti, L. Pino, H. Mirzaian, E.J. Taylor, G. Wilemski, Morphological characteristics of ptfe bonded gas diffusion electrodes, Electrochim. Acta. 36 (1991) 1049.
[11] D.M. Bernardi, W.M. Verbrugge, Mathematical model of a gas diffusion electrode bonded to a polymer electrolyte, AIChE 37 (1991) 1151–1163.
[12] E.A. Ticianelli, C.R. Derouin, A. Redondo, S. Srinivasan, Methods to advance technology of proton exchange membrane fuel cells, J. Electrochem. Soc. 135 (1988) 2209–2214.
[13] E.A. Ticianelli, C.R. Derouin, S. Srinivasan, Localization of platinum in low catalyst loading electrodes to attain high power densities in SRE fuel cells, J. Electroanal. Chem. 251 (1988) 275–295.
[14] V. Gurau, H.T. Liu, S. Kakac, Two dimensional model for proton exchange membrane fuel cells, AIChE J. 44 (1998) 2410–2422.
[15] T.F. Fuller, J. Newman, Water and heat management in solid-polymer-electrolyte fuel cell, J. Electrochem. Soc. 140 (1993) 1218–1225.
[16] T.V. Nguyen, R.E. White, A water and heat management model for proton-exchange membrane fuel cells, J. Electrochem. Soc. 140 (1993) 2178–2186.
[17] J.S. Yi, T.V. Nguyen, An along-the-channel model of PEM Fuel cells, J Electrochem. Soc. 145 (1998) 1149–1159.
[18] J.S. Yi, T.V. Nguyen, Multi-component transport in porous electrodes of proton exchange membrane fuel cells using inerdigitated gas distributors, J. Electrochem. Soc. 146 (1999) 38–45.
[19] S. Shimpalee, S. Dutta, Effect of Humidity on PEM Fuel Cell Performance Part-II Numerical Simulation, HTD-Vol. 364-1, Heat Transfer Division, ASME, 1999.
[20] T. Zhou, H. Liu, A general three-dimensional model for proton exchange membrane fuel cells, I. J. Trans. Phenomena 3 (3) (2001) 177–198.
[21] S. Um, C.Y. Wang, Computational fluid dynamics modeling of proton exchange membrane fuel cells, J. Electrochem. Soc. 147 (12) (2000) 4485–4493.
[22] S. Um, C.Y. Wang, Three dimensional analysis of transport and reaction in proton exchange membrane fuel cells, in: Proceedings of the ASME Fuel Cell Division The 2000 ASME IMECE Nov. 5–10, Walt Disney World Dolphin, Orlando, FL.
[23] T.C. Jen, Simultaneously Developing Laminar Convection in the Entrance Region of a Semi-porous Channel, HTD-Vol. 275 ASME, 1994, pp. 111–122.
[24] S.V. Patankar, Numerical Heat transfer and fluid flow, Hemisphere, Washington, DC, 1980.
[25] K. Vafai, C.L. Tien, Boundary and inertial effects on flow and heat transfer in porous media, Int. J. Heat Mass Transfer 24 (1981) 152–169.
[26] A. Parthasarathy, S. Srinivasan, A.J. Appleby, Temperature dependence of the electrode kinetics of oxygen reduction at the Platinum/Naflon interface-a microelectrode investigation, J. Electrochem. Soc. 139 (1992) 2530.
[27] T.E. Springer, T.A. Zawodinski, S. Gottesfeld, Polymer electrolyte fuel cell model, Electrochem. Soc. 136 (1991) 2334–2341.
[28] B. Farouk, T. Fusegi, Predictions of fluid and heat transfer problems by the vorticity–velocity formulation of the Navier–Stokes equations, J. Comput. Phys. 65 (1986) 227–243.
[29] F.C. Chou, G.J. Hwang, Vorticity–velocity method for the graetz problem and the effect of natural convection in a horizontal rectangular channel with uniform wall heat flux, J. Heat Transfer 109 (1987) 704–710.
[30] T.C. Jen, A.S. Lavine, Laminar heat transfer and fluid flow in the entrance region of a rotating duct with rectangular cross section: The effect of aspect ratio, J. Heat Transfer 114 (1992) 574–581.
[31] R.H. Shah, A.L. London, Laminar Flow Forced Convection in Ducts, Academic Press, New York, 1978.
[32] R.M. Curr, D. Sharma, D.G. Tatchell, Numerical prediction of some three-dimensional boundary layers in ducts, Comput. Meth. Appl. Mech. Engng. 1 (1972) 143–158.
[33] D.M. Bernardi, M.W. Verbrugge, A mathematical model of the solid-polymer-electrolyte fuel cell, J. Electrochem. Soc. 139 (9) (1992) 2477–2491.